Diverse Roles of Metal Ions in Acyl-Transferase Ribozymes†

Anand Vaidya and Hiroaki Suga*

Department of Chemistry, State University of New York at Buffalo, Buffalo, New York 14260-3000

Received February 7, 2001; Revised Manuscript Received March 23, 2001

ABSTRACT: The dependence on metal ions for catalysis is one of the hallmark characteristics of ribozymes. Yet despite this universal reliance, the functional role of divalent ions in promoting RNA catalysis is manifold. In this study we elucidate some different roles metal ions play as catalytic cofactors, by comparing two functionally co-evolved acyl-transferase ribozymes. Earlier studies performed on the in vitro selected acyl-transferase ribozyme, E18 [Suga, H., Cowan, J. A., and Szostak, J. W. (1998) *Biochemistry 28,* 10118−10125], revealed the requirement of a fully hydrated (outer-sphere) Mg^{2+} ion for catalytic activity. Interestingly, one class of acyl-transferase ribozymes isolated from the same RNA pool as E18 displays a unique metal dependency and is believed to be interacting with inner-sphere coordinated Mg^{2+} ions. New results show that one of these inner-sphere coordinating ribozymes, HS01, assumes a cloverleaf secondary structure closely resembling E18, yet apparently facilitates a distinct catalytic mechanism. Furthermore, the nature of the RNA−metal interaction(s) in HS01 seems to be dictating a unique reaction mechanism that exhibits a titratable moiety at a near-neutral pK_a. In light of the critical role metal ions play in biochemistry and the proper function of RNAs, these results compare two distinct manners by which metals serve to promote the catalysis of the same reaction.

The past 2 decades have witnessed a surging interest into the catalytic nature of naturally occurring ribozymes (*1*−*3*). The phosphodiester transfer reaction catalyzed by the majority of these ribozymes has been critically examined in numerous studies, resulting in an improved understanding of their catalytic mechanism and metal ion dependence (*4*, *5*). Despite the fact that all naturally occurring ribozymes rely on metal ions for activity, it has become clear that the interactions and catalytic functions of these metals exhibit great diversity.

The phosphodiester cleavage reaction in the hammerhead ribozyme involves an inner-sphere coordinated metal that serves to activate the 2′-OH of the ribose ring (*4*, *6*−*12*). Hammerhead chemistry also includes a metal acting as a Lewis acid by binding to the *pro-*R_p nonbridging oxygen (and the leaving group) at the site of cleavage (*11*−*15*). In another example, the Tetrahymena ribozyme is suspected to require the interactions of three inner-sphere coordinated divalent ions to assist in its self-splicing reaction (*16*−*22*). The adaptive involvement of divalent ions is further illustrated in the hairpin ribozyme, where studies have shown that rather than acting as Lewis acids, outer-sphere coordinated metal ions play an important role in the proper folding required for hairpin ribozyme chemistry (*23*, *24*). Moreover, recent studies have expanded the catalytic functions assumed by metals by proposing the possibility of their participation in the general acid−base catalysis defining the hepatitis delta virus ribozyme's activity (*25*−*27*).

The RNA tertiary structure environment is likely to influence variations in metal ion coordination modes and mechanisms. The secondary structures of the naturally occurring ribozymes mentioned above are distinct from one another, making it difficult to correlate exactly how structure dictates catalytic metal dependence or vice versa. To effectively study the varying roles assumed by metals in RNA catalysis, an ideal setting would entail examining structurally and functionally similar ribozymes with unique metal-dependent behaviors.

Since it is well-known that many in vitro evolved ribozymes are able to catalyze reactions other than phosphodiester transfer, we can investigate the diversity of RNA catalysis using a platform of nonnaturally occurring ribozymes. Acyl-transferase ribozymes (Figure 1) represent practical substitutes for studying the varying metal dependence of naturally occurring ribozymes, because the acyl-transfer reaction is chemically analogous to the phosphodiester reaction, with the sp^3 phosphorus replaced by an sp^2 carbonyl carbon. In the past, we have structurally and kinetically characterized an in vitro selected acyl-transferase ribozyme, E18, and shown that catalysis was mediated by outer-sphere interactions of a divalent or trivalent metal ion with the ribozyme's active site (*28*, *29*).

Here we report structural and mechanistic studies on a new acyl-transferase ribozyme, HS01. This ribozyme was isolated from the same RNA pool as E18 (*30*); however, it was only selected when more stringent selection conditions were applied. Although the structural similarities between HS01 and E18 are clearly evident, it appears that the functional

† This research was supported by ACS Grant PRF-33938-G4 and NSF Grant MCB-9982237 to H.S. A.V. is a recipient of the P. Lansbury Fellowship (awarded by the Department of Chemistry, SUNY at Buffalo) and the Barry M. Goldwater Scholarship.

* To whom correspondence should be addressed. E-mail: hsuga@acsu.buffalo.edu.

10.1021/bi0102757 CCC: $20.00
Published on Web 05/24/2001

role and coordination state of metal ions involved with HS01 differ significantly from those of E18. Our study focuses on characterizing this new ribozyme and attempting to decipher how unique aspects of HS01 differentiate its metal ion dependence from E18.

EXPERIMENTAL PROCEDURES

In Vitro Selection. The RNA pool in round 10, which was previously selected by Lohse and Szostak (*30*), was subjected to more stringent selection conditions, where the RNA pool was incubated for 1 min with 1 μM *N*-biotinylated methionyl-3′-ACCAAC-5′ substrate (5′-CAACCA-3′-Met-Biotin)[1] at pH 6.8 in the presence of 10 mM Mg^{2+}, than the previous conditions (3 min with 5 μM substrate at pH 7.3 in the presence of 50 mM Mg^{2+}). The remaining selection procedures were the same as those previously reported. After three rounds of selection, the streptavidin-dependent gel-mobility-shift assay (vide infra) showed that approximately 15% of the total input of RNA was self-aminoacylated. The RT/PCR-amplified DNA template of this RNA pool was cloned into pGEM-T vector systems (Promega), and 20 clones were sequenced by standard methods. The sequences were aligned using CLUSTALW sequence alignment (http://pbil.ibcp.fr/cgi-bin/npsa_automat.pl?page=/NPSA/npsa_server.html), and classified based on the similarity of sequences.

Ribozyme Synthesis. Ribozymes were synthesized and labeled by T7 RNA polymerase runoff transcription of PCR DNA templates (clone HS01) in the presence of [α-^{32}P]UTP. For mutant ribozymes, the DNA template coding for HS01 was amplified by PCR in the presence of appropriate primers to introduce mutations or deletions. The transcripts were treated with RNase-free DNase for 20 min. Products were purified by denaturing polyacrylamide gel electrophoresis and were eluted from the gel into 0.3 M NaCl. The ethanol-precipitated RNA was dephosphorylated by treatment with calf intestinal phosphatase, and the product was isolated by phenol−chloroform extraction, and ethanol precipitation. The pellet was then resuspended in DEPC (diethyl pyrocarbonate)−water.

Cleavage Assays. Full-length unlabeled HS01 RNA, prepared by T7 RNA polymerase runoff transcription of PCR DNA templates, was 5′-labeled in the presence of [γ-^{32}P]-ATP by T4 polynucleotide kinase. A 9 μL RNA solution containing 0.1 μM 5′-labeled HS01, 25 mM MOPS, and 100 mM KCl buffered at pH 7.5 was prepared for cleavage reactions in the absence of Mg^{2+}, and 8 μL RNA solutions were prepared for those reactions to be conducted in the presence of Mg^{2+}. The solutions were heat-denatured at 95 °C for 2 min and allowed to sit at 25 °C for 5 min. To the samples to be cleaved in the presence of Mg^{2+} was added 1 μL of either 100 mM or 500 mM $MgCl_2$ and allowed to equilibrate at 25 °C for 5 min. Cleavage was initiated by the addition of 1 μL of 5 mM $Pb(OAc)_2$ or $TbCl_3$, and incubated for 30−120 min at 25 °C. Reactions were quenched by the addition of 10 μL of quenching buffer (70 mM EDTA, 8 M urea), followed by ethanol precipitation. Cleavage fragments were separated by 10% PAGE and visualized using a Bio-Rad Molecular Imager FX.

General Kinetic Protocol. Acyl-transfer reactions were carried out as follows: An 8 μL ribozyme solution containing 1.5 μM ribozyme, 100 mM KCl, and 25 mM EPPS at pH 8.0 was prepared. The solution was heat-denatured at 95 °C for 2 min, and incubated at 25 °C for 5 min. To this solution was added 1 μL of 100 mM divalent metal, and the mixture was incubated for 5 min at 25 °C. In the case of the $Co(NH_3)_6^{3+}$ competition assay, varying amounts of $Co(NH_3)_6^{3+}$ dissolved in water containing 1 mM EDTA were added to a 7 μL ribozyme solution after folding the ribozyme in the presence of 10 mM $MgCl_2$. Reactions were initiated by the addition of 1 μL of 40 μM 5′-CAACCA-3′-Met-Biotin to the ribozyme solution. Determination of K_M and k_{cat} values was achieved by adding 1 μL of varying substrate concentrations rather than a fixed value. To stop the reactions, 1 μL aliquots of the reaction mixture were periodically extracted and quenched in 4 μL of a quenching buffer containing 8 M urea, 70 mM EDTA, 42 μM streptavidin, and 50 mM Tris·HCl adjusted to pH 6.0. Reaction samples were analyzed by 6% PAGE at 4 °C, and the bands were resolved using the Molecular Imager. Titration data were fitted using the KaliedaGraph graphing and curve-fitting package (Abelbeck Software).

Metal Titration Experiments. Metal(II) chlorides ($MgCl_2$, $MnCl_2$, $CaCl_2$, $CoCl_2$, $CuCl_2$, $ZnCl_2$, and $CdCl_2$) were dissolved in distilled water to prepare 0.1 M stock solutions. Cobalt(III) hexammine was dissolved in water containing 1 mM EDTA to prepare a 0.1 M stock solution. An 8 μL ribozyme solution was prepared containing 1.5 μM ribozyme with 100 mM KCl buffered in 25 mM EPPS at pH 8.0, or 25 mM MOPS at pH 6.7. The solution was denatured at 95 °C for 2 min, and then allowed to sit at 25 °C for 5 min. To this solution was added 1 μL of various concentrations of metal(II) chloride solution, and the mixture was incubated for 5 min at 25 °C. Reactions were initiated by the addition of 1 μL of 40 μM Biotin-Met-3′-ACCAAC-5′ substrate to the samples. The remaining procedures were performed as described in the general kinetic protocol.

pH-Dependent Kinetics. Buffers were made of MES (pH 5.5−5.9), PIPES (pH 6.2−6.5), MOPS (pH 6.7−7.7), and EPPS (pH 8.0−8.56). RNA solutions were prepared with the appropriate buffers as mentioned in the general kinetic protocol, except that a final concentration of 5 mM $MgCl_2$ or $MnCl_2$ was added in solution with 1 mM spermidine. The remaining procedures were carried out as described in the general kinetic protocol.

RESULTS AND DISCUSSION

In Vitro Selection of New Classes of Acyl-Transferase Ribozymes. Our previously reported in vitro selection scheme resulted in the isolation of only one dominant class of acyl-transferase ribozyme (*28*, *30*). This ribozyme is able to transfer a biotinylated methionyl (Biotin-Met) group from the 3′-end of a substrate hexanucleotide (5′-CAACCA-3′) to a hydroxyl or amino group at its own 5′-end (Figure 1A). The secondary structure of this class of ribozymes was determined (*28*), and the acyl-transfer mechanism of one

[1] Abbreviations: ATP, adeonsine triphosphate; DEPC, diethyl pyrocarbonate; EDTA, ethylenediaminetetraacetic acid; EPPS, *N*-(2-hydroxyethyl)piperazine-*N*′-3-propanesulfonic acid; IGS, internal guide sequence; MES, 4-morpholineethanesulfonic acid monohydrate; Met, methionine; MOPS, 3-(*N*-morpholino)propanesulfonic acid; PAGE, polyacrylamide gel electrophoresis; PCR, polymerase chain reaction; PIPES, 1,4-piperazinebis(ethanesulfonic acid); RT, reverse transcription; SAv, streptavidin; UTP, uracil triphosphate.

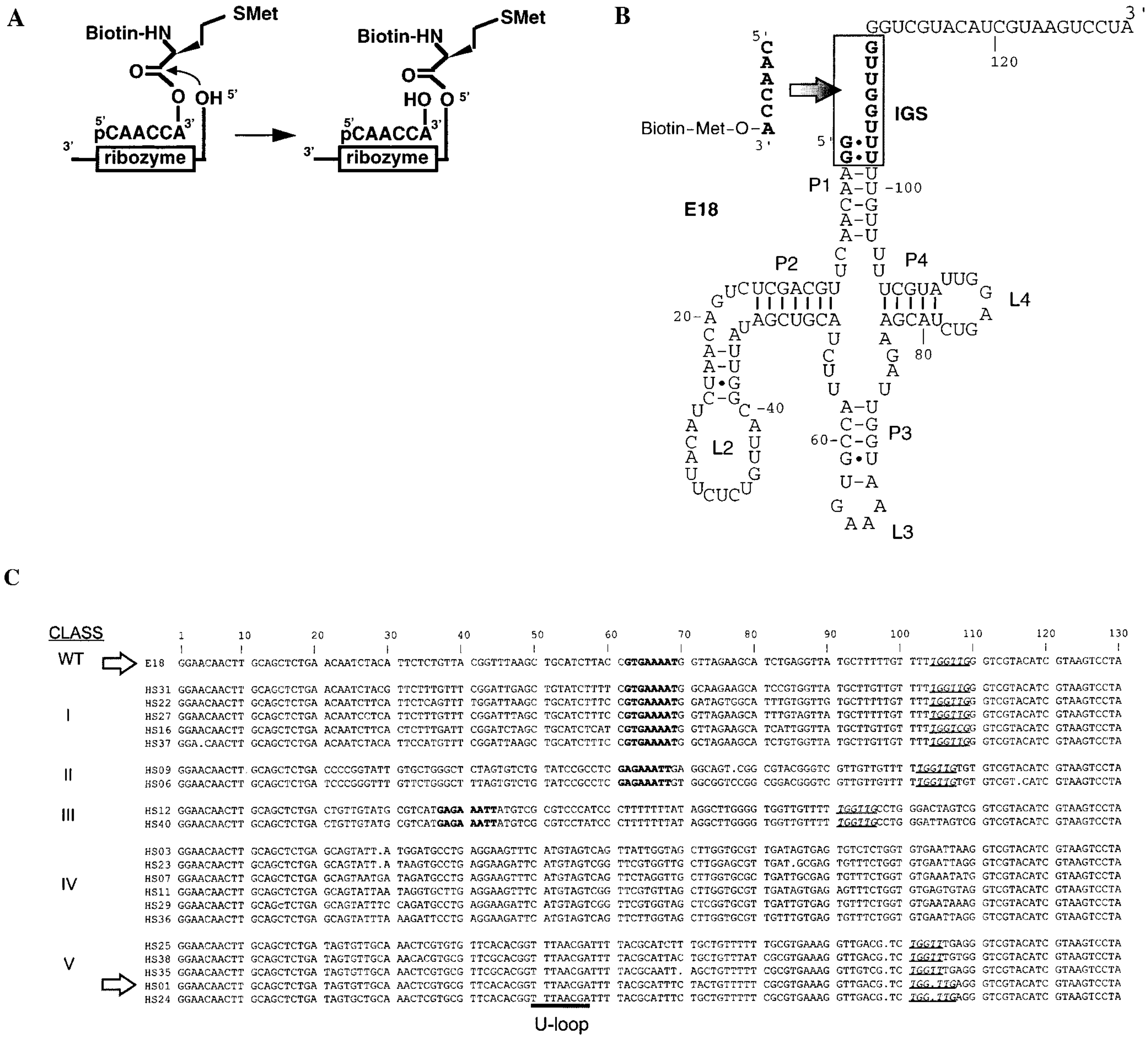

FIGURE 1: Representation of full-length E18 and new classes of in vitro selected ribozymes. (A) Schematic of the catalyzed acyl-transferase reaction. The 5′-CAACCA-3′ hexanucleotide is charged with a biotinylated methionine group at its 3′-end (5′-CAACCA-3′-Met-Biotin). The oligonucleotide binds to a complementary 5′-UGGUUG-3′ (IGS) sequence on the ribozyme, and the biotinylated amino acid is transferred to the 5′-OH of the ribozyme. (B) Full-length secondary structure of E18. The IGS is boxed and highlighted in boldface type, as are the tandem G·U wobble base pairs which constitute the binding site for a hexahydrate Mg^{2+} ion. (C) Sequence alignment of the selected clones shown in comparison to the wild-type E18. Five independent classes are depicted, although Class I is of the same class as E18. The underlined italics highlight the IGS sequence which is present in E18, Classes I−III, and Class V, while arrows denote the E18 and HS01 sequences. In E18 and Classes I−III, the boldface lettering depicts the commonly shared GAAA loop motif enclosed by a stem containing a G·U wobble base pair, while the underline in Class V represents the nucleotides constituting the U-loop.

representative clone, E18, was dissected (Figure 1B). The studies revealed that E18 required a single catalytic metal ion in the fully hydrated form for activity (*29*). Strong support for this coordination was obtained by using $Co(NH_3)_6^{3+}$ as an effective substitute for Mg^{2+}. On the basis of metal-dependent kinetic studies conducted on the wild-type and mutant E18 ribozymes, we concluded that the tandem G·U wobble base pairs near the acylation site most likely constitute the catalytic metal binding site (*31, 32*), and play an essential role in accelerating the acyl-transfer reaction.

Since dependence on outer-sphere metal interactions is fairly unique among ribozymes characterized to date (*4*), we wondered whether outer-sphere coordination was the only mechanism that could support the acyl-transfer reaction. To explore this possibility, we subjected the 10th-round pool RNA (*30*) to increased selective pressures, with the aim of generating novel classes of active sequences with unique metal-dependent behaviors (see Experimental Procedures). After three rounds of stringent selection at a lower pH, Mg^{2+} concentration, and incubation time, the population of RNA present in the resulting pool displayed an enhanced sequence diversity. These ribozymes were categorized into five independent classes (I−V) of ribozymes based on their primary sequence similarities (Figure 1C). It should be noted that E18 belongs to the Class I ribozymes as defined by the sequence alignment.

Although the primary sequences of Classes I−V are distinguished by their different genotypes, ribozymes in

Classes II and III share some characteristic structural and sequence features as those in Class I: the formation of tandem G•U wobble base pairs near the acylation site, and the formation of a GAAA loop that is enclosed by a stem containing a G•U wobble base pair (A. Flynn-Charlebois, N. Lee, and H. Suga, unpublished result). These common traits suggest that the ribozymes in Classes I−III probably employ similar reaction mechanisms. In fact, the ribozymes in Classes I−III are all able to maintain comparable acyltransferase rates when $Co(NH_3)_6^{3+}$ is substituted for Mg^{2+}, indicative of the conservation of outer-sphere RNA−metal interactions. On the other hand, Class IV ribozymes do not possess the above characteristic motifs, yet they are capable of sustaining comparable activity with $Co(NH_3)_6^{3+}$ (H. Suga, unpublished results).

Interestingly, Class V ribozymes, whose primary sequences diverge considerably from Classes I−IV, are catalytically inert in the presence of $Co(NH_3)_6^{3+}$. This observation suggests that the catalytic role of Mg^{2+} in this subset of ribozymes differs from that of E18 and the ribozymes in the other four classes. In light of this disparity, we decided to further investigate one of these Class V clones, HS01, to specifically evaluate the mechanistic and structural attributes distinguishing the metal dependency of HS01 from E18.

Metal-Mediated Cleavage and Structural Resolution of HS01. To effectively compare HS01 and E18, we aimed to first resolve the secondary structure of HS01. Like E18, HS01 contains a 5′-UGGUUG-3′ internal guide sequence (IGS), which is complementary to the 5′-CAACCA-3′-Met-Biotin substrate. However, since the remainder of the HS01 sequence deviates considerably from E18, prediction of stem and loop regions was achieved by analyzing chemical digests of HS01.

The ability of Pb^{2+} and Tb^{3+} hydroxides to severe the RNA backbone at structurally accessible regions has been used to map the correct structures of several large RNAs, thereby establishing metal-mediated RNA cleavage as a useful method by which to resolve secondary structure (*33*−*38*). S1 nuclease provides further insight on structural loops and bulges, as it specifically degrades single-stranded RNA endonucleolytically. Thus, in an initial attempt to determine the correct conformation for HS01, we approached the matter using Pb^{2+}, Tb^{3+}, and S1 nuclease, as chemical and enzymatic probes.

The S1 cleavage pattern of HS01 in the absence of any Mg^{2+} (but with 100 mM KCl) is identical to that observed in the presence of 10 mM Mg^{2+} (and 100 mM KCl), with major cleavage sites appearing at U52−A54, U59−A62, A66−U80, A87−G90, and U103−U104 (Figure 2A, lanes 1 and 2). The general Pb^{2+} and Tb^{3+} hydrolysis results in the absence of any Mg^{2+} show significant cleavage at U18−U21, A32−C35, U42−C45, U50−U52, G56−U61, A66−C81, G86−U93, C96−C99, and G102−U103, reflecting an overlap with many of the same cleavage sites observed with S1 nuclease (Figure 2B, lanes 3 and 6).

In the absence of Mg^{2+}, both Pb^{2+} and Tb^{3+} display unique cleavage profiles within and around the IGS (U100−G105) as well as at the U50−U52 region: Pb^{2+} readily cleaves U50−U52, G97−C99, and G102−U103, while Tb^{3+} does not demonstrate specific cleavage of U50−U52, but shows major hydrolysis at C96−C99 and less intense cleavage at G102−U103 (Figure 2B, lanes 3 and 6). Because the remaining Pb^{2+} and Tb^{3+} cleavage patterns are consistent, the variance in Pb^{2+} and Tb^{3+} cleavage specificity observed around the IGS and U50−U52 regions suggests that the hydrolysis of these sites may be related to the size or specific binding preferences of the individual metal hydroxide ions.

Based on our S1 nuclease and metal cleavage mapping results, and the aid of the Zuker algorithm (*39*), we derived a reasonable secondary structure for HS01 (Figure 2D). The regions prone to metal hydrolysis and S1 cleavage correspond with loops or junction regions in our secondary structure, with the exception of the metal cleavage seen within P4, which is probably due to the weak base-pairing nature of the stem.

By inducing mutations that would either confirm or deny the existence of particular structural attributes present in our proposed configuration of HS01, we tested the validity of this secondary structure. The catalytic role of the proposed L5 stem−loop was examined by truncating HS01 immediately 3′ to the IGS (deletion of 106−128). This truncated mutant (HS01-truncated) displayed a mild 1.4-fold decrease in activity when compared to wild-type HS01, thereby affirming the relative unimportance of the 3′-tail in catalysis (Table 1, entries 1 and 2). In addition, we assessed the role of the L2 (U18−U22) and L4 (A66−C81) loop regions of HS01-truncated by replacing them with stable tetraloops, hence generating two mini-HS01 mutants. The mini-L4-HS01 mutant (containing a single substitution of L4 to a UUCG-tetraloop) displayed a rate 1.6-fold greater than the wild-type full-length HS01. The mini-L2-L4-HS01 mutant (containing a double substitution of L2 and L4 to GAGA- and UUCG-loops, respectively) displayed a rate 1.3-fold greater than the mini-L4-HS01 mutant (Table 1, entries 3 and 9). The removal of the proposed L2 and L4 loop regions resulted in a slight increase in HS01's activity, implying that their deletion does not disrupt the active structure of HS01, and furthermore that neither of the loops are vital in promoting catalysis.

The postulated HS01 secondary structure has uncanny resemblances to E18 (Figure 3). Previous chemical probing experiments and mutational studies have determined that the full-length E18 structure (Figure 1B) can be truncated to a compact cloverleaf structure, STE18, more recently named ATRib (Figure 3B) (*28*, *40*). Our recent structural analyses on STE18 have revealed that neither L2 nor L4 is vital for catalysis: both loops can be substituted with stable tetraloops (A. Flynn-Charlebois and H. Suga, unpublished results). The secondary structure of mini-L2-L4-HS01 represents a cloverleaf structure containing remarkable similarities to STE18, with the noteworthy appearance in HS01 of a small loop between P3 and P4 (referred to as the U-loop) and bulged loops near the 5′-end and IGS in P1 (Figure 3A). Though A3−A4 and A95−G97 are depicted as forming a small bulged loop in P1 of HS01, it is very probable that these bases are highly structured (perhaps via noncanonical base-pairing), since single-strand probes, such as S1 and Pb^{2+}, reveal no cleavage at A95−G97.

Identifying Metal Binding Sites. The specific cleavage of the phosphodiester backbone by Pb^{2+}, and more recently by Tb^{3+}, hydroxide ions has been used to identify high-affinity metal binding sites in RNAs (*4*, *9*, *10*, *38*, *41*, *42*). These ions have been established as efficient probes for detecting Mg^{2+} binding sites because, in addition to having a prefer-

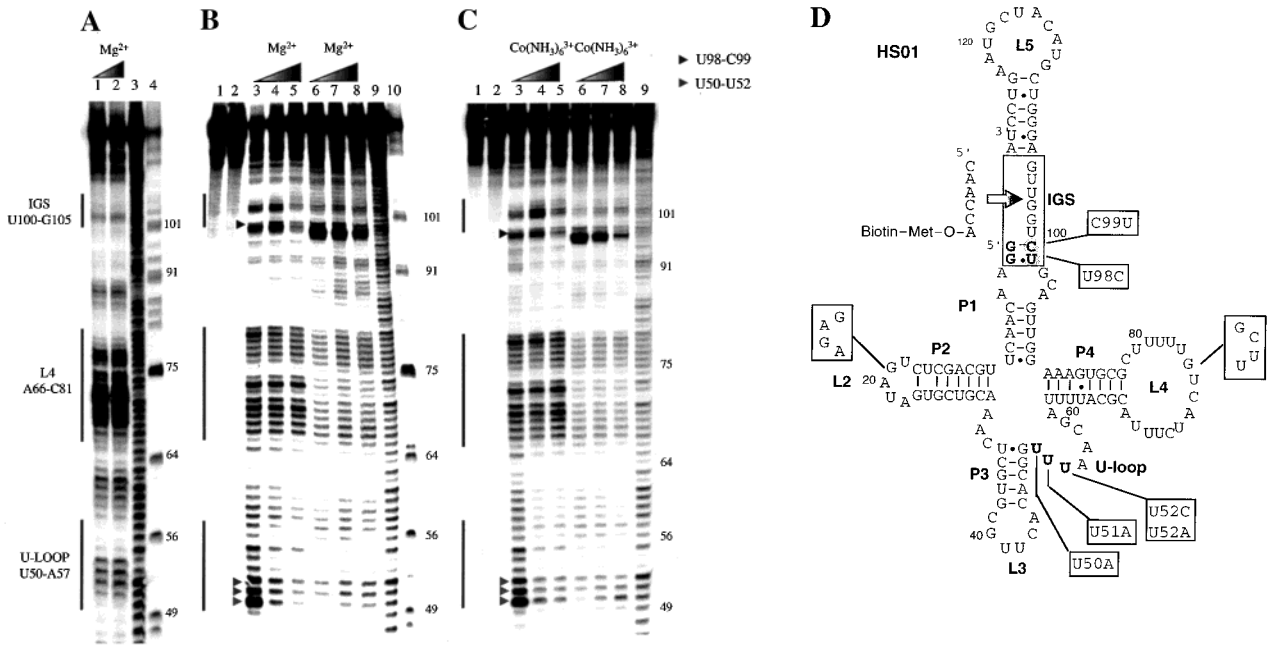

FIGURE 2: Secondary structure determination of HS01. Key structural regions are marked alongside the gels by vertical lines, while significant nucleotides for discussion are marked by arrowheads. Note that the use of Pb^{2+}, Tb^{3+}, and S1 probes cleaves the bridging phosphate between two nucleotides, forming a 2′,3′-cyclic phosphate at the 3′-end of one nucleotide, and a hydroxyl group at the 5′-end of the other nucleotide. (A) Cleavage induced by S1 nuclease digests. Lane 1 depicts an S1 cleavage pattern of HS01 in the absence of any Mg^{2+} ions. Lane 2 shows the S1 cleavage of HS01 in the presence of 10 mM Mg^{2+} ion. The hydrolysis patterns of both lanes 1 and 2 are alike, with no apparent differences. Lanes 3 and 4 represent an alkaline hydrolysis and a T1 ladder, respectively. (B) Pb^{2+} and Tb^{3+} cleavage sites in full-length HS01, with competition by Mg^{2+} ions. Lanes 1 and 2 are controls: lane 1 is HS01 in water, while lane 2 is a control showing cleavage of HS01 under cleavage conditions with 10 mM Mg^{2+} as described under Experimental Procedures, however without the addition of any Pb^{2+} or Tb^{3+}. Lanes 3−5 show Pb^{2+} cleavage patterns in the presence of 0.5 mM $Pb(OAc)_2$. The Mg^{2+} concentrations are increased progressively from 0 to 10 to 50 mM. Lanes 6−8 represent the Tb^{3+} cleavage results in the presence of 0.5 mM $TbCl_3$. As in the case of lanes 3−5, the Mg^{2+} concentrations are increased stepwise from 0 to 10 to 50 mM for the three Tb^{3+} cleavage samples. Lane 9 is an alkaline hydrolysis, and lane 10 is a T1 ladder. The cleavage time under different Mg^{2+} concentration conditions has been adjusted so that comparable lanes have regions of constant cleavage intensity, thereby enabling the efficient comparison of regions where protection of cleavage is seen. (C) Pb^{2+} and Tb^{3+} cleavage sites in full-length HS01 with competition by $Co(NH_3)_6^{3+}$ ions. Lanes 1 and 2 are controls akin to those in (B), except that lane 2 has 10 mM $Co(NH_3)_6^{3+}$ rather than Mg^{2+}. Lanes 3−5 show Pb^{2+} cleavage analogous to that described in (B), with $Co(NH_3)_6^{3+}$ concentrations increasing stepwise from 0 to 1 to 10 mM. Lanes 6−8 show Tb^{3+} hydrolysis sites analogous to those in (B), with concentrations increasing as in lanes 3−5. (D) Secondary structure of full-length HS01, including further induced mutations. The IGS is in boldface, and regions that were deleted or point-mutated to create HS01 mutants are represented in gray.

Table 1: Relative Rates of Reaction of HS01 Mutants

entry	mutant	incorporated point mutations	rate relative to HS01 WT	rate relative to mini-L4-HS01
1	HS01 WT		1.000	
2	HS01 truncated		0.730	
3	mini-L4-HS01		1.600	1.000
4		U50A + U51A		0.009
5		U52C		0.079
6		U52A		0.310
7		C99U		0.030
8		U98C		0.580
9	mini-L2-L4-HS01			1.300

ence for coordinating oxygen ligands, their hydrates have near-neutral pK_a's, thus enabling them to compete for Mg^{2+} binding sites and hydrolyzing the phosphodiester backbone at a physiological pH.

Interestingly, when HS01 was folded in the presence of increasing Mg^{2+} concentrations, Pb^{2+} hydrolysis was observed to be considerably competed at U50−U52 and at the sites adjacent to the IGS (G97−C99 and G102−U103), while Tb^{3+}-mediated cleavage was mildly diminished at sites around the IGS (C96−C99 and G102−U103) (Figure 2B, lanes 4−5 and 7−8). This noteworthy competition of hydrolysis by increased Mg^{2+} concentrations, while other cleavage patterns remain unchanged, suggests that the cleaved regions within and adjacent to the IGS as well as U50−U52 are potential metal binding sites.

The U-loop is a small bulge appearing between L3 and L4 of HS01, and containing a U-stretch (U50−U52) at the 5′-end of the loop. Though S1 nuclease digests show mild cleavage at A53−A57 of this U-loop, the inhibition of S1 cleavage at U50−U52 under all conditions tested suggests that the tertiary involvement of this region of the loop always protects it from strand scission by the bulky nuclease (Figure 2A, lanes 1 and 2). Pb^{2+} cleavage at U50−U52 in the absence of Mg^{2+} is very prominent, but is drastically inhibited as Mg^{2+} concentrations are elevated to 50 mM. This strong Mg^{2+}-induced protection of U50−U52 from Pb^{2+} hydrolysis is indicative of a Mg^{2+} binding site that Pb^{2+} is able to access and readily cleave only in the absence of competition by Mg^{2+} ions.

Mutational probing of the U-loop reveals its influence on catalytic activity: the double mutations of U50A and U51A resulted in a decrease in activity greater than 110-fold when compared to mini-L4-HS01 (Table 1, entry 4), while the single mutations U52C and U52A resulted in a 13-fold and 3-fold drop in activity, respectively (entries 5 and 6), when compared to the mini-L4-HS01 (entry 3). The ribozyme's

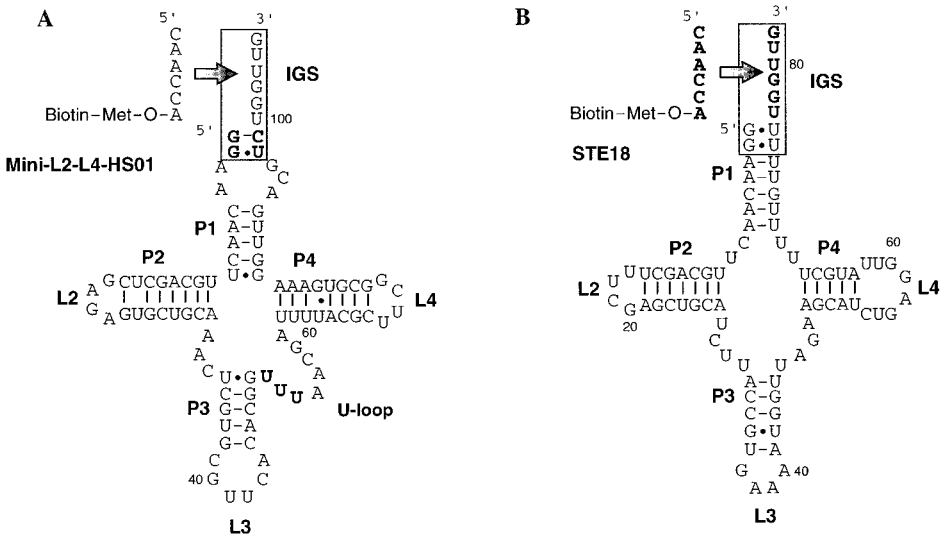

FIGURE 3: Structural comparison of E18 and HS01. (A) Secondary structure of mini-L2-L4-HS01. (B) Secondary structure of STE18 (truncated E18).

reliance on this U50−U52 region is testament to the vital role of the U-loop in promoting catalysis, and indirectly supports the assumption that it represents an essential element in forming a Mg^{2+} binding site.

The protection of Pb^{2+}- and Tb^{3+}-mediated hydrolysis of the bases within and adjacent to the IGS, as Mg^{2+} concentrations increase, provides evidence for a potential Mg^{2+} binding motif near the active site (Figure 2B, lanes 4−5 and 7−8) (*38*, *41*). The U98 and C99 adjacent to the IGS are heavily cleaved by Pb^{2+}, and especially Tb^{3+}, yet are noticeably protected in the presence of 50 mM Mg^{2+}, suggesting that Mg^{2+} interacts with HS01 in such a way as to protect these two bases from metal hydrolysis. To assess the importance of these bases, we introduced single mutations to mini-L4-HS01, U98C, and C99U, and examined their effect on catalytic rate. The former mutation resulted in a 2-fold decay in activity, whereas the latter reduced activity by more than 30-fold (Table 1, entries 7 and 8). This result suggests that the C99U mutation disrupts either metal interactions or the structural architecture of the active site, to considerably depress activity.

It is apparent from Figure 2B that Mg^{2+} is able to effectively displace Pb^{2+} from U50−U52, as well as competing with both Pb^{2+} and Tb^{3+} at nucleotides G97−C99 adjacent to the IGS. The cleavage of U50−U52 is restricted to Pb^{2+} hydrolysis, and is not observed in the presence of Tb^{3+}, suggesting that the size, or ligand preference, of the metal ion involved is a principal factor governing the metal interaction with the U-loop. One hypothesis explaining the observed phenomenon, which is elaborated upon in subsequent sections, is that nucleotides G98−C99 interact with U50−U52, forming a concerted metal binding pocket. From the Mg^{2+} competition results, Pb^{2+} ions are clearly binding to a Mg^{2+} binding site in the vicinity of G98−C99; however, cleavage is also seen at the presumably nearby interacting bases: U50−U52. Hydrated Tb^{3+} ions (0.92 Å) have an ionic radius more comparable to hydrated Mg^{2+} (0.72 Å), and have a higher positive charge and smaller radius than Pb^{2+} ions (1.19 Å). As a result, the Tb^{3+} hydroxides bind strongly to the metal binding site at G98−C99, but are unable to cleave the nearby U-loop due to their smaller spatial size and high affinity for functional groups within the G98−C99 region, and perhaps simply due to the lack of perferred ligands within the U-loop.

Incentive to prefer the single metal binding site model stems from the observation that a Hill cooperativity analysis of a Mg^{2+} titration in the presence of spermidine has implicated the involvement of a single catalytic metal ion in HS01's reaction chemistry (vide infra). Understanding the exact nature, or even existence, of an interaction between U50−U52 and G97−C99 with metal ions (Mg^{2+}, Pb^{2+}, and Tb^{3+}) requires more detailed investigations; however, the drastic decline of k_{obs} when mutations are induced to either U50−U52 or G97−C99 establishes their crucial role in catalysis (Table 1). More insight into the nature of the metal binding site(s) is shed in the sections below.

STE18 has been well-characterized as forming tandem G·U wobble base pairs involving the 5′-end G1−G2 and U75−U76 adjacent to the IGS (Figure 3B) (*29*). The proposed HS01 secondary structure places the 5′-nucleophile in the proximity of the IGS by base-pairing G1−G2 with U98−C99, in a similar fashion as STE18 (Figures 2B,D and 3). The G·U wobble base pairs in E18 have been identified as the probable metal binding site for hydrated metal ions such as $Mg(H_2O)_6^{2+}$ and $Co(NH_3)_6^{3+}$ (*31*, *32*); however, a similar role of the G1−C99 and G2−U98 pairs in HS01 is debatable. This assumption is supported by the fact that the mutation C99U, which in theory should form tandem G·U base-pairing analogous to the STE18 catalytic core (Figure 3B), resulted in a tremendous reduction of activity in the presence of Mg^{2+} (Table 1, entry 7). Furthermore, the C99U mutant could not support activity in the presence of $Co(NH_3)_6^{3+}$ (data not shown), implying that the tandem G·U wobble base pairs were not supporting a hydrated metal binding site as seen with STE18, and confirming that HS01 cannot support the same catalytic mechanism as STE18. Even though both ribozymes seem to share an active site Mg^{2+} bound directly adjacent to the IGS, the varying architecture of the metal binding site differentiates the metal dependence of each ribozyme.

In STE18, the tandem G·U pairs are next to a very stable helix of five base pairs in P1. In contrast, the C99U mutant

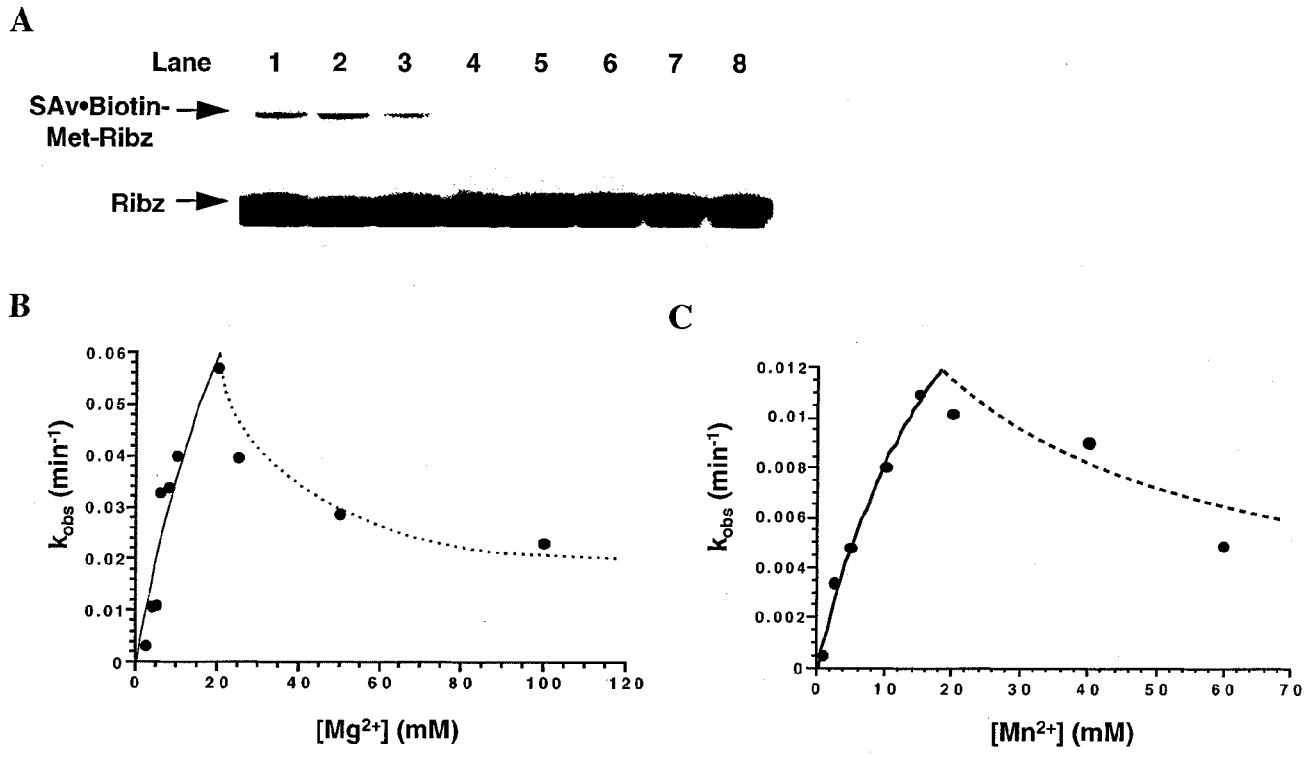

FIGURE 4: Metal dependency of the acyl-transfer reaction catalyzed by HS01. (A) Metal ion dependence of HS01 [lane 1 = Mg^{2+}, 2 = Mn^{2+}, 3 = Ca^{2+}, 4 = Co^{2+}, 5 = Cu^{2+}, 6 = Zn^{2+}, 7 = Cd^{2+}, 8 = $Co(NH_3)_6^{3+}$]. Acyl-transfer reactions were carried out in the presence of 10 mM metal chloride, in 100 mM KCl and 25 mM EPPS, pH 8.0 for 2 min. Mobility shifts indicating active species are due the binding of streptavidin to the biotin attaced to the methionyl group. (B) Catalytic activity of HS01 versus Mg^{2+} concentration and (C) Mn^{2+} concentration. Dashed lines are not associated with any mathematical function; rather they are smooth extrapolations of data points, since we are still unsure of the exact inhibitory mechanism.

of HS01 places these tandem G·U pairs next to an unstable asymmetric internal loop (A3−A4, A95−G97). The instability of this motif in HS01 may be preventing the closure of the internal loop, and hence inhibiting the formation of tandem G·U wobble base pairs and a complete P1 helix. Maintaining the P1 helix is desirable because the hexanucleotide substrate must bind directly adjacent to, and coaxially stack, on the double-stranded P1 helix, thus propagating the helix by another six nucleotides. In the C99U mutant of HS01, the G1−U99 pair may be so unstable that even Mg^{2+} coordination cannot propagate P1 helix formation past the C5−G94 pair. As a result, the substrate would have to find the IGS without the help of stabilizing effects such as coaxial stacking and helix propagation. The C99 nucleotide in HS01 was most probably selected for this reason: to favor the closure of the internal loop in P1, and hence provide stability for a metal binding site and substrate docking.

Divalent Metal Ion Dependency. Since HS01 was isolated from a Mg^{2+}-dependent selection, the prospect of it exhibiting activity in the presence of other divalent metal species was yet to be verified. Examining the kinetics of HS01, by measuring the acyl-transfer rate as a function of the 5′-CAACCA-3′-Met-Biotin concentration, revealed a Michaelis−Menten relationship with a K_m of 2.7 ± 0.5 μM and a k_{cat} of approximately 0.04 ± 0.004 min^{-1}. Acyl-transfer activity was observed in the presence of different metal ions under near-saturating substrate conditions (see Experimental Procedures). Of the various divalent metal ions tested, only Ca^{2+} and Mn^{2+}, in addition to Mg^{2+}, were able to sustain activity, while no activity was observed in the presence of other assorted transition metals: Co^{2+}, Cu^{2+}, Zn^{2+}, and Cd^{2+} (Figure 4A).

Given that the electronic configuration and chemical affinity of Mg^{2+} and Mn^{2+} are representative of two different periodic groups (alkaline earth vs transition), the activity of HS01 was scrutinized exclusively in the presence of Mg^{2+} and Mn^{2+} in order to compare their individual effects on catalysis. The metal dependency of HS01 at pH 8.0 is distinct from E18, as the maximum rate of reaction is 5-fold faster in the presence Mg^{2+} over Mn^{2+} (Figure 4B,C), whereas prior data on E18 show a 30-fold difference in maximum rate between Mg^{2+}- and Mn^{2+}-dependent catalysis. In the case of Mg^{2+}, the k_{obs} is seen to rise with increasing metal concentrations until it reaches a peak at 20 mM (Figure 4B). Likewise, the reaction rate is enhanced with increasing Mn^{2+} concentrations prior to reaching a maximum at 15 mM (Figure 4C). In both cases, increasing the metal ion concentration beyond the point of maximal activity resulted in a drop in the acyl-transfer rate.

Since excess manganese hydroxides have been known to precipitate out of solution at higher pH, we examined the same Mn^{2+} titration at pH 6.7. Though the maximum acylation activity is reduced at pH 6.7 due to the hydroxyl dependency of the reaction, the rate profile is still analogous to the titration at pH 8.0 (data not shown). This result suggests that the observed decline in activity at higher Mn^{2+} concentrations (Figure 4C) is not due to the formation of metal polyhydroxide precipitates, but rather to an inhibitory mechanism that is activated by a threshold concentration of metal ion (as also seen in the case of Mg^{2+}) (Figure 4B).

Inhibition is apparently only witnessed when metal concentrations are raised high enough to fully saturate the catalytic binding site, implying that an inhibitory site having a lower affinity toward Mg^{2+} and Mn^{2+} in comparison to the catalytic binding site exists.

The existence of an inhibition site(s) in HS01, with low affinity toward Mg^{2+} and Mn^{2+} ions, accounts for why our stringent selection scheme resulted in the isolation of Class V ribozymes. The original selection for acyl-transfer ribozymes was conducted at a Mg^{2+} concentration of 50 mM. As mentioned in the in vitro selection section above, at this Mg^{2+} concentration only one class of E18-like ribozymes was isolated, and all of these clones exhibited near-maximum rates at 50 mM Mg^{2+} concentration (*29*). From our metal titration results, we clearly see that at a 50 mM Mg^{2+} concentration, the k_{obs} of HS01 is approximately at half of its maximal value (Figure 4B), and approximately 10-fold lower than that of E18 (data not shown). Thus, the presence of 50 mM Mg^{2+} in the original selection was responsible for the inhibitory effect that prevented the isolation of the Class V clones, as their activity was greatly depressed compared to E18-like clones. However, when only 10 mM Mg^{2+} was used in the ensuing stringent selection, the result was the emergence of four new classes, including Class V and HS01, whose maximal acyl-transfer rate is witnessed at Mg^{2+} concentrations ranging around 20 mM (Figure 4B).

It should be noted that the Hill analysis performed on the titration data in the presence of 0.5−10 mM Mg^{2+} (pH 8.0) and Mn^{2+} (pH 6.7) resulted in Hill coefficients of 1.39 and 1.72, respectively, thus denoting the involvement of more than one metal ion. Much of the observed Pb^{2+} and Tb^{3+} hydrolysis occurs at regions of nonspecific metal binding sites, such as the L4 region, which are not competed for by increasing Mg^{2+} concentrations. By adjusting the cleavage time for each Mg^{2+} concentration, nonspecific sites of hydrolysis, such as L4, are visualized with approximately constant intensities, whereas specific cleavage sites are seen to be competed with increasing Mg^{2+} concentration (Figure 2). When 1 mM spermidine was added to replace these nonspecific Mg^{2+} ions, the reaction profile for k_{obs} vs concentration of Mg^{2+} and Mn^{2+} resembled the profiles observed in the absence of spermidine (data not shown). Hill analysis on the data points representing the initial rise in catalytic activity in the presence of spermidine yielded cooperativity coefficients of 1.00 and 1.17, respectively, for Mg^{2+} and Mn^{2+}. Thus, in the presence of spermidine, our Hill analysis focuses only on specifically involved metal ions, suggesting that HS01 likely requires only one catalytic metal ion for activity.

Metal Ion Coordination and Inhibition Studies. Understanding how divalent ions coordinate to the ribozyme is meaningful when trying to decipher the essential role of the metal ions in catalysis. Past evidence has shown that E18, HS01's functional and evolutionary counterpart, is able to fully support acyl-transfer activity in the presence of Co-$(NH_3)_6^{3+}$ (*29*). An octahedral geometry and essentially negligible ligand exchange allow $Co(NH_3)_6^{3+}$ to mimic a fully hydrated divalent metal ion, $M(H_2O)_6^{2+}$, thereby affording the opportunity to evaluate the sphere of interaction by which catalytic metals associate with RNA (*43, 44*). The ability of E18 to exhibit comparable rates of catalysis with Mg^{2+} and $Co(NH_3)_6^{3+}$ provided convincing support that the catalytic Mg^{2+} coordinated with the ribozyme via outer-sphere interactions.

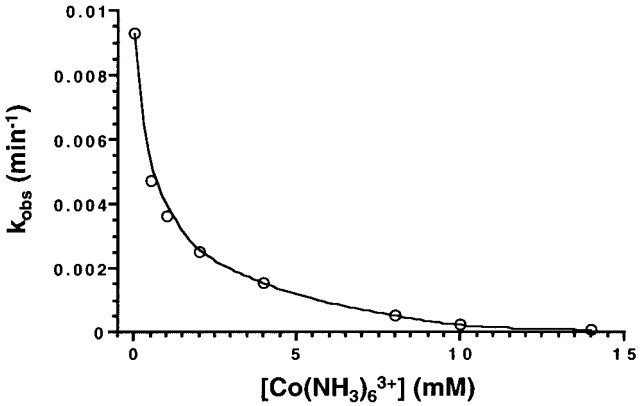

FIGURE 5: Cobalt(III) hexammine inhibition assay. Depression of HS01 catalytic activity in the presence of 10 mM Mg^{2+}, as increasing concentrations of $Co(NH_3)_6^{3+}$ are added.

To investigate the interaction of the critical divalent ion in HS01, we considered its activity in the presence of Co-$(NH_3)_6^{3+}$. When $Co(NH_3)_6^{3+}$ replaced Mg^{2+} and Mn^{2+}, all acyl-transfer activity was lost, suggesting that HS01 is unable to catalyze the acyl transfer in the presence of strictly outer-sphere-mediated interactions (Figure 4A, lane 8). $Co(NH_3)_6^{3+}$ ions may inhibit HS01 activity by competing with Mg^{2+} for the catalytic binding site, or by binding elsewhere on the ribozyme to efficiently deactivate it. To resolve this issue, the acyl-transfer rate was observed by titrating increasing amounts of $Co(NH_3)_6^{3+}$ in the presence of 10 mM Mg^{2+}. As depicted in Figure 5, the presence of $Co(NH_3)_6^{3+}$ severely inhibits the acyl-transfer reaction, as catalytic activity is depressed to half-maximal rate at only 0.5 mM $Co(NH_3)_6^{3+}$.

The inhibitory relationship displayed by HS01 is in stark contrast to that exhibited by E18 in past studies, where both Mg^{2+} and $Co(NH_3)_6^{3+}$ were shown to support catalysis. The synergistic behavior displayed by Mg^{2+} and $Co(NH_3)_6^{3+}$ in competition assays performed on E18 suggested that both species promote the reactivity of the ribozyme through the same binding site (*29*). However, the opposing effects of Mg^{2+} and $Co(NH_3)_6^{3+}$ on HS01's activity suggest either that both ions occupy the same site but only Mg^{2+} can use its ligand versatility to catalyze the reaction, or that $Co(NH_3)_6^{3+}$ inhibits activity by binding at some other location on the ribozyme.

Support for an inhibitory mechanism(s) was originally seen in the Mg^{2+} and Mn^{2+} titrations (Figure 4B,C), where acylation activity was observed to gradually decay at elevated concentrations of Mg^{2+} and Mn^{2+}. As exemplified by the results of the metal titration and competition assays, Mg^{2+} and Mn^{2+} ions can effectively promote and inhibit the activity of HS01, while $Co(NH_3)_6^{3+}$, with its fixed octahedral geometry, only influences the inhibition of the ribozyme, although with a seemingly higher affinity than the divalent ions (*45*). The drastic decline in activity witnessed at low concentrations of $Co(NH_3)_6^{3+}$ upholds the notion of an inhibitory site that is mediated strictly by outer-sphere interactions.

Horton et al. similarly observed two types of metal sites in the hammerhead ribozyme by performing $Co(NH_3)_6^{3+}$ inhibition studies (*13, 45*). The catalytic metal site of the

hammerhead requires inner-sphere coordination, whereas a separate inhibitory site binds $Co(NH_3)_6^{3+}$via outer-sphere interactions to cause an unfavorable structural conformation (*6*). In the case of the hammerhead, even though activity was slowed due to $Co(NH_3)_6^{3+}$ binding, some catalytic activity was maintained via inner-sphere binding of divalent ions to the distinct active site (*45*).

To decipher whether the inhibitory site and the catalytic site in HS01 were one in the same, or two separate binding locations, Pb^{2+} and Tb^{3+} hydrolyses were performed in the presence of competition by $Co(NH_3)_6^{3+}$ (Figure 2C). The resulting cleavage profile was akin to that observed previously with increasing Mg^{2+} concentrations; cleavage by Pb^{2+} is profoundly inhibited by increasing $Co(NH_3)_6^{3+}$ concentrations at the sites adjacent to IGS and at U50−U52, and Tb^{3+} hydrolysis is significantly decreased at C96−C99, adjacent to IGS. This observation demonstrates that $Co(NH_3)_6^{3+}$ competes with Pb^{2+} and Tb^{3+} for the same sites as Mg^{2+}. It also clearly shows that $Co(NH_3)_6^{3+}$ inhibits cleavage near the IGS and at U50−U52 far more strongly than Mg^{2+}, implying that $Co(NH_3)_6^{3+}$ binds to these sites with a higher affinity than Mg^{2+}.

Our cleavage results clearly show two specific metal binding sites that are both competed for by Mg^{2+} as well as $Co(NH_3)_6^{3+}$; however, the Hill analysis in the presence of spermidine indicates the involvement of only one specific metal ion. In light of these observations, we can extrapolate that both sites of Mg^{2+} and $Co(NH_3)_6^{3+}$ competition actually represent a single binding motif in tertiary space. Hence, nucleotides U50−U52 likely associate with U98−C99 and cooperatively constitute a single binding site for the catalytic metal ion.

Considering the framework of this single metal binding site, why does an excess amount of Mg^{2+}, as well as $Co(NH_3)_6^{3+}$, inhibit the ribozyme's activity (Figures 4B and 5)? We currently believe that at low concentrations of Mg^{2+} (below 20 mM), a single Mg^{2+} ion binds to the above-mentioned cooperative metal binding site consisting of U50−U52 and U98−C99, and the active conformation of the ribozyme is achieved. However, at higher concentrations of Mg^{2+} (above 20 mM), excess ions bind independently to both sites, thus disrupting the crucial interaction between U50−U52 and U98−C99, and effectively inhibiting HS01 activity (Figure 4B). Similarly, when excess $Co(NH_3)_6^{3+}$ is added to an active HS01 population in the presence of Mg^{2+}, it binds to either U50−U52 or U98−C99, or possibly to both sites. Due to its inability to exchange ligands, $Co(NH_3)_6^{3+}$ prevents the progression of the acyl-transfer reaction as well as blocking access to Mg^{2+}, thus inhibiting the rate as seen in Figure 5. Although we believe that this proposal for an inhibitory mechanism best fits our data presently, more extensive experiments will certainly be required to build a more definitive and resolved explanation.

pH-Dependent Kinetics. Kinetic assays under variable pH conditions were carried out on HS01 to gain insights into the titratable participants of catalysis. The acyl-transfer reaction was carried out at varying pHs under fixed substrate and metal concentrations (5 mM Mg^{2+} and Mn^{2+}). Upon plotting log k_{obs} against pH, analogous hyperbolic titration curves were observed for both ions (Figure 6A,B). HS01's acyl-transferase ability exhibits linear hydroxide ion dependence with increasing pH, followed by a plateau of log k_{obs} where the rate becomes pH-independent. In the case of both plots, the slope of the linear region is nearly 1 (0.81 and 0.86, respectively, for Mg^{2+} and Mn^{2+}), consistent with the fact that only one rate-limiting ionization transpires during catalysis (Figure 6A,B).

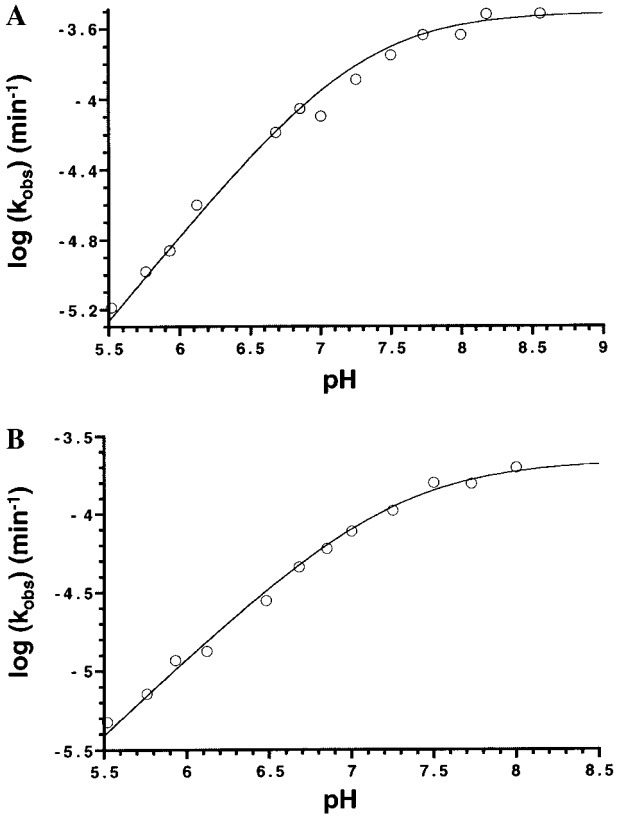

FIGURE 6: pH dependence of the acyl-transfer reaction in the presence of (A) 5 mM Mg^{2+} and (B) 5 mM Mn^{2+}. Data points are best fit to the equation: $k_{obs} = k_{obs}^{max} - \log[1 + (10^{M0})/(10^{-pH})]$, yielding a p$K_a$ value of 7.25 ± 0.05 for Mg^{2+} and 7.24 ± 0.05 for Mn^{2+}.

To confirm that the pH-dependent behavior witnessed was independent of the concentration of metal ion, we performed the same pH titration of k_{obs} at a lower divalent metal concentration. The titration behavior was identical when the concentrations of Mg^{2+} and Mn^{2+} were reduced to 1 mM from 5 mM, implying that the pH-dependent behavior of HS01 is independent of divalent metal concentration (data not shown).

The observed pK_as of the ionizable groups in the presence of Mg^{2+} or Mn^{2+} were 7.25 ± 0.05 and 7.24 ± 0.05, respectively. The unperturbed pK_as of water molecules bound to Mg^{2+} or Mn^{2+} are 11.4 and 10.6, respectively, approximately 5 orders of magnitude more basic than the pK_a values we obtained (*4*, *7*). Analogous pK_a perturbations have recently been observed in the hepatitis delta virus ribozyme and the 23S ribosomal RNA subunit, and have been attributed to a general acid−base catalysis mechanism involving a titratable nucleotide and an interacting metal ion (*25*, *27*, *46*−*48*).

Efficient acid−base catalysis requires ionizable participants to have a pK_a around pH 7.0, which is in accord with our titration data of HS01 (*47*). Since ribonucleotide functional groups in RNA bases do not have pK_as near neutrality, we

postulate that the influence of metal ions, and/or particular RNA residues, perturbs the pK_a of an active site functional group in HS01 toward neutrality, thereby facilitating its participation in catalysis. The fact that HS01 titrates at a neutral pK_a, deviating significantly from the pK_a of a water-bound Mg^{2+} or Mn^{2+}, suggests that we may have titrated a functional group involved in an acid−base mechanism playing a critical role regulating catalysis, similar to that observed in naturally occurring ribozymes (*26*, *27*, *46*).

Remarkably, the same pH-dependent kinetics previously performed on E18 did not reveal any titratable groups in the range of pH 6.5−8.0, as the pH-dependent plots displayed a linear relationship with a slope of 1 (*29*). The lack of any ionizable functionality in E18 eliminates the possibility of its participation in any acid−base chemistry, and subsequently suggests a significant disparity between the catalytic mechanisms of HS01 and E18.

CONCLUSION

The discussed results demonstrate the versatility of metal ions in supporting the catalysis of two co-evolved ribozymes, E18 and HS01. Since both ribozymes catalyze the identical acyl-transfer reaction, and are now considered to have homologous secondary structures, the variance in metal dependence and coordination reveals a glimpse of the diverse assortment of roles metals can undertake as catalytic cofactors.

From our results on HS01, we propose the existence of one specific metal binding site near the 5′-OH nucleophile and IGS, which is formed by the concerted interactions of nucleotides U50−U52 with U98−C99. This site appears to have a high affinity for inner-sphere coordinating metals such as Mg^{2+}, which serve to promote catalysis at low concentrations. At higher concentrations, excess Mg^{2+} ions are observed to inhibit the activity of HS01 by presumably disrupting the arrangement of the active site. In a similar fashion, $Co(NH_3)_6^{3+}$ binds with HS01 at the same general sites as Mg^{2+}, but due to its constrained geometry and inability to exchange ligands, its presence inhibits the activity of HS01.

In E18, a fully hydrated metal bound at the tandem G•U wobble base pairs adjacent to the IGS and the 5′-OH is believed to favor catalysis by stabilizing the oxyanion transition state of the acylation reaction (*29*). In contrast, the inner-sphere divalent ion in HS01, which is also positioned in the proximity of the IGS and the 5′-OH, may be participating in the chemistry governing the reaction by perturbing the pK_a of some undetermined functional group to a near-neutral pH.

To further investigate our findings, we are currently attempting to transcriptionally incorporate a 5′-thio-5′-deoxyguanosine analogue at the 5′-end of HS01. The substitution of a 5′-SH nucleophile for a 5′-OH can be useful in determining the interaction of metal ions with the 5′-nucleophile, by observing changes in the pK_a of the acyl-transfer reaction due to the specific affinities of Mg^{2+} and Mn^{2+} for oxygen and sulfur groups (*20*, *49*). We also hope to gain further insights into the titratable participant(s) and structural architecture of HS01 by conducting modification and nucleotide analogue interference mapping experiments (*46*, *50*).

ACKNOWLEDGMENT

Acknowledgment is made to the donors of the Petroleum Research Fund administered by the ACS and to the National Science Foundation (both awarded to H.S.) for support of this research. Special thanks is given to Thomas Barnes III for his critical readings and valued suggestions. We also thank Dr. Janet Morrow and the members of the Suga lab for their helpful discussions.

REFERENCES

1. Pyle, A. M. (1993) *Science 261*, 709−714.
2. Lilley, D. M. (1999) *Curr. Opin. Struct. Biol. 9*, 330−338.
3. Hanna, R., and Doudna, J. A. (2000) *Curr. Opin. Chem. Biol. 4*, 166−170.
4. Feig, A. L., and Uhlenbeck, O. C. (1999) in *The RNA World* (Gesteland, R. F., Cech, T. R., and Atkins, J. F., Eds.) 2nd ed., pp 287−319, Cold Spring Harbor Laboratory Press, Cold Spring Harbor, NY.
5. McKay, D. B., and Wedekind, J. E. (1999) in *The RNA World* (Gesteland, R. F., Cech, T. R., and Atkins, J. F., Eds.) 2nd ed., pp 287−319, Cold Spring Harbor Laboratory Press, Cold Spring Harbor, NY.
6. Cunningham, L. A., Li, J., and Lu, Y. (1998) *J. Am. Chem. Soc. 120*, 4518−4519.
7. Dahm, A. C., and Uhlenbeck, O. C. (1991) *Biochemistry 30*, 9464−9469.
8. Dahm, A. C., Derrick, W. B., and Uhlenbeck, O. C. (1993) *Biochemistry 32*, 13040−13045.
9. Feig, A. L., Scott, W. G., and Uhlenbeck, O. C. (1998) *Science 279*, 81−84.
10. Scott, W. G., Murray, J. B., Arnold, J. R. P., Stoddard, B. L., and Klug, A. (1996) *Science 274*, 2065−2069.
11. Zhou, D.-M., Zhang, L.-H., and Taira, K. (1998) *Proc. Natl. Acad. Sci. U.S.A. 94*, 14343−14348.
12. Pontius, B. W., Lott, W. B., and von Hippel, P. H. (1997) *Proc. Natl. Acad. Sci. U.S.A. 94*, 2290−2294.
13. Wang, S., Karbstein, K., Peracchi, A., Beigelman, L., and Herschlag, D. (1999) *Biochemistry 38*, 14363−14378.
14. Ruffner, D. E., and Uhlenbeck, O. C. (1990) *Nucleic Acids Res. 18*, 6025−6029.
15. Scott, E. C., and Uhlenbeck, O. C. (1999) *Nucleic Acids Res. 27*, 479−484.
16. Sugimoto, N., Kierzek, R., and Turner, D. H. (1988) *Biochemistry 27*, 6384−6392.
17. Li, Y., and Turner, D. H. (1997) *Biochemistry 36*, 11131−11139.
18. McConnell, T. S., Herschlag, D., and Cech, T. R. (1997) *Biochemistry 36*, 8293−8303.
19. Shan, S., Yoshida, A., Sun, S., Piccirilli, J. A., and Herschlag, D. (1999) *Proc. Natl. Acad. Sci. U.S.A. 96*, 12299−12304.
20. Piccirilli, J. A., Vyle, J. S., Caruthers, M. H., and Cech, T. R. (1993) *Nature 361*, 85−88.
21. Weinstein, L. B., Jones, B. C., Cosstick, R., and Cech, T. R. (1997) *Nature 388*, 805−808.
22. Shan, S. O., and Herschlag, D. (2000) *RNA 6*, 795−813.
23. Hampel, A., and Cowan, J. A. (1997) *Chem. Biol. 4*, 513−517.
24. Butcher, S. E., Allain, F. H.-T., and Feigon, J. (2000) *Biochemistry 39*, 2174−2182.
25. Shih, I. H., and Been, M. D. (1999) *RNA 5*, 1140−1148.
26. Perrotta, A. T., Shih, I.-H., and Been, M. D. (1999) *Science 286*, 123−126.
27. Nakano, S., Chadalavada, D. M., and Bevilacqua, P. C. (2000) *Science 287*, 1493−1497.
28. Suga, H., Lohse, P. A., and Szostak, J. W. (1998) *J. Am. Chem. Soc. 120*, 1151−1156.
29. Suga, H., Cowan, J. A., and Szostak, J. W. (1998) *Biochemistry 37*, 10118−10125.
30. Lohse, P. A., and Szostak, J. W. (1996) *Nature 381*, 442−444.
31. Cate, J. H., and Doudna, J. A. (1996) *Structure 4*, 1221−1229.

32. Kieft, J. S., and Tinoco, J. I. (1997) *Structure 5*, 713−721.
33. Krzyzosiak, W. J., Marciniec, T., Wiewiorowski, M., Romby, P., Ebel, J. P., and Giege, R. (1988) *Biochemistry 27*, 5771−5777.
34. Pan, T., Gutell, R. R., and Uhlenbeck, O. C. (1991) *Science 254*, 1361−1364.
35. Zito, K., Huttenhofer, A., and Pace, N. R. (1993) *Nucleic Acids Res. 21*, 5916−5920.
36. Ciesiolka, J., Hardt, W. D., Schlegl, J., Erdmann, V. A., and Hartmann, R. K. (1994) *Eur. J. Biochem. 219*, 49−56.
37. Winter, D., Polacek, N., Halama, I., Streicher, B., and Barta, A. (1997) *Nucleic Acids Res. 25*, 1817−1824.
38. Sigel, R. K., Vaidya, A., and Pyle, A. M. (2000) *Nat. Struct. Biol. 7*, 1111−1116.
39. Mathews, D. H., Sabina, J., Zuker, M., and Turner, D. H. (1999) *J. Mol. Biol. 288*, 911−940.
40. Lee, N., Bessho, Y., Wei, K., Szostak, J., and Suga, H. (2000) *Nat. Struct. Biol. 7*, 28−33.
41. Hargittai, M. R., and Musier-Forsyth, K. (2000) *RNA 6*, 1672−1680.
42. Walter, N. G., Yang, N., and Burke, J. M. (2000) *J. Mol. Biol. 298*, 539−555.
43. Black, C. B., Huang, H.-W., and Cowan, J. A. (1994) *Coord. Chem. Rev. 135/136*, 165−202.
44. Cowan, J. A. (1997) in *Inorganic Biochemistry. An introduction*, Wiley-VCH, New York.
45. Horton, T. E., and DeRose, V. J. (2000) *Biochemistry 39*, 11408−11416.
46. Muth, G. W., Ortoleva-Donnelly, L., and Strobel, S. A. (2000) *Science 289*, 947−950.
47. Cech, T. R. (2000) *Science 289*, 878−879.
48. Nissen, P., Hansen, J., Ban, N., Moore, P. B., and Steitz, T. A. (2000) *Science 289*, 920−930.
49. Yoshida, A., Sun, S., and Piccirilli, J. A. (1999) *Nat. Struct. Biol. 6*, 318−321.
50. Strobel, S. A. (1999) *Curr. Opin. Struct. Biol. 9*, 346−352.

BI0102757